



In situ controlled rapid growth of novel high activity $\text{TiB}_2/(\text{TiB}_2\text{-TiN})$ hierarchical/heterostructured nanocomposites

Jilin Wang¹, Hejie Liao¹, Yuchun Ji¹, Fei Long^{*1}, Yunle Gu², Zhengguang Zou¹, Weimin Wang^{*3} and Zhengyi Fu³

Full Research Paper

[Open Access](#)

Address:

¹School of Materials Science and Engineering, Key Laboratory of Nonferrous Materials and New Processing Technology of Ministry of Education, Guilin University of Technology, Guilin 541004, China, ²Nano and Ceramic Materials Research Center, Wuhan Institute of Technology, Wuhan 430073, China, and ³The State Key Laboratory of Advanced Technology for Materials Synthesis and Processing, Wuhan University of Technology, Wuhan 430070, China

Email:

Fei Long^{*} - longf@glut.edu.cn; Weimin Wang^{*} - shswmwang@whut.edu.cn

* Corresponding author

Keywords:

chemical activity; hierarchical/heterostructures; self-propagating high-temperature synthesis; TiB_2 ; TiN

Beilstein J. Nanotechnol. **2017**, *8*, 2116–2125.

doi:10.3762/bjnano.8.211

Received: 16 May 2017

Accepted: 18 September 2017

Published: 10 October 2017

Associate Editor: J. J. Schneider

© 2017 Wang et al.; licensee Beilstein-Institut.

License and terms: see end of document.

Abstract

In this work, a reaction coupling self-propagating high-temperature synthesis (RC-SHS) method was developed for the in situ controlled synthesis of novel, high activity $\text{TiB}_2/(\text{TiB}_2\text{-TiN})$ hierarchical/heterostructured nanocomposites using TiO_2 , Mg, B_2O_3 , KBH_4 and NH_4NO_3 as raw materials. The as-synthesized samples were characterized using X-ray diffraction (XRD), scanning electron microscope (SEM), X-ray energy dispersive spectroscopy (EDX), transition electron microscopy (TEM), high-resolution TEM (HRTEM) and selected-area electron diffraction (SAED). The obtained TiB_2/TiN hierarchical/heterostructured nanocomposites demonstrated an average particle size of 100–500 nm, and every particle surface was covered by many multibranched, tapered nanorods with diameters in the range of 10–40 nm and lengths of 50–200 nm. In addition, the tapered nanorod presents a rough surface with abundant exposed atoms. The internal and external components of the nanorods were TiB_2 and TiN, respectively. Additionally, a thermogravimetric and differential scanning calorimetry analyzer (TG-DSC) comparison analysis indicated that the as-synthesized samples presented better chemical activity than that of commercial TiB_2 powders. Finally, the possible chemical reactions as well as the proposed growth mechanism of the $\text{TiB}_2/(\text{TiB}_2\text{-TiN})$ hierarchical/heterostructured nanocomposites were further discussed.

Introduction

Refractory materials such as borides, nitrides and carbides have attracted great attention for advanced engineering applications due to their exceptional hardness, thermal and chemical stability

at high temperatures [1-3]. For example, titanium diboride (TiB_2) processes high hardness and a high melting point, good chemical and metallurgical stability, as well as excellent elec-

trical and thermal conductivity [4-6]. On the other hand, titanium nitride (TiN) has some attractive properties, such as high hardness, low electrical resistivity, excellent wear and corrosion resistance [1,2,7]. Therefore, it is expected that these unique properties will make TiB₂/TiN composites an attractive prospect for practical applications in many fields such as super-hard materials, electrodes, wear resistance materials, armor plates, jet engine parts and high temperature ceramic components [1,3,7,8].

The previous researches were primarily focused on the preparation and performance of TiB₂/TiN composite ceramics or films. However, there are few reports about the preparation of the raw powders of TiB₂/TiN composites. It is common knowledge that high activity powders are the indispensable prerequisite for the preparation of the corresponding composites with distinguished properties [9,10]. Thus, in our opinion, the understanding of the fabrication of homogeneously dispersed, high activity TiB₂/TiN nanocomposite powders is of great importance.

As for the preparation of TiB₂/TiN composite powders, the common synthesis routes are combustion synthesis methods and high-energy ball milling assisted methods with heat treatment using Ti, B, BN and TiH₂ as raw materials [1-3,11-13]. Based on the previous works, it is known that the high-energy ball milling assisted heat treatment method requires long milling time (30–40 h) and high energy consumption. In addition, although the combustion synthesis method is suitable for industrialized production of inorganic ceramic powders, the raw materials used in this method are expensive. Even more remarkable, the TiB₂/TiN composite powders synthesized by these two above-mentioned preparation methods also display conventional particle morphology.

Recently, several kinds of inorganic nanomaterials have been prepared in our research group using a developed reaction coupling self-propagating high-temperature synthesis (RC-SHS) technology [9,10,14]. The results showed that the heat of the reaction intensity, morphology, purity, particle size and dispersibility of the samples could be controlled through changing the coupling reaction (endothermic reaction) ratio. Given the current problems regarding the preparation of TiB₂/TiN composite powders, based on our previous research idea, the production of distinctive TiB₂/TiN products synthesized via this RC-SHS method are desired.

In this paper, we propose an effective method for the in situ controlled, rapid synthesis of novel TiB₂/(TiB₂-TiN) hierarchical/heterostructured nanocomposites via the RC-SHS method. The phase, element composition, morphology, microstructure and chemical activity of the as-synthesized products

were investigated in detail by various characterization methods. In addition, further comparative experiments were carried out to study the relation between the endothermic reaction rate and the morphology/microstructure/composition of the samples. Moreover, based on the obtained experimental results and previous work, the possible chemical reactions as well as the appropriate growth mechanism of the TiB₂/(TiB₂-TiN) hierarchical/heterostructured nanocomposites were also discussed.

Results and Discussion

Figure 1a,b gives the typical field emission scanning electron microscope (FSEM) images of the as-prepared TiB₂/(TiB₂-TiN) samples where the endothermic rate is 40%. It is obvious that the samples demonstrated interesting hierarchical structures which were composed of grains and short rods. In detail, these grains revealed particle sizes of about 100–500 nm. The surface of the grain was covered by many tapered nanorods with a diameter of 10–40 nm and a length of 50–100 nm (indicated by arrows). In addition, the grain that was originally located at the center of the hierarchical structure eventually disappeared completely and transformed into a scattering multibranch structure (marked with frame). Moreover, hierarchical structures were well-distributed without agglomeration. The corresponding X-ray energy dispersive spectroscopy (EDX) spectrum (Figure 1c) reveals significant elemental B, Ti, N and O. The existence of O could be attributed to the surface hydrolysis and oxidation of the hierarchical structures. Figure 1d displays the typical X-ray diffraction (XRD) pattern of the as-prepared TiB₂/(TiB₂-TiN) samples where the endothermic rate is 40%. Nine peaks could be assigned to characteristic planes of TiB₂ (JCPDF card No.65-1073) [15]. The other four peaks could be indexed to corresponding planes of TiN (JCPDF card No.65-5774) [16]. Additionally, the peaks of other byproducts, such as MgO, were not detected in this pattern.

Figure 2a–c presents typical transition electron microscopy (TEM) images of the as-prepared TiB₂/(TiB₂-TiN) samples where the endothermic rate is 40%. Figure 2a shows a low magnification image, and Figure 2b,c show high-magnification images. The sizes of solid grains were in the range of 100–200 nm. The nanorods also displayed solid structures with a length of 50–150 nm and tapering diameters from 5 nm to 30 nm.

In order to further determine the internal microstructure and phase constitution of the as-synthesized samples, the high-resolution transition electron microscopy (HRTEM) (Figure 2d,f) and selected-area electron diffraction (SAED) (Figure 2e,g) analysis of the tapered nanorods and grains was performed, re-

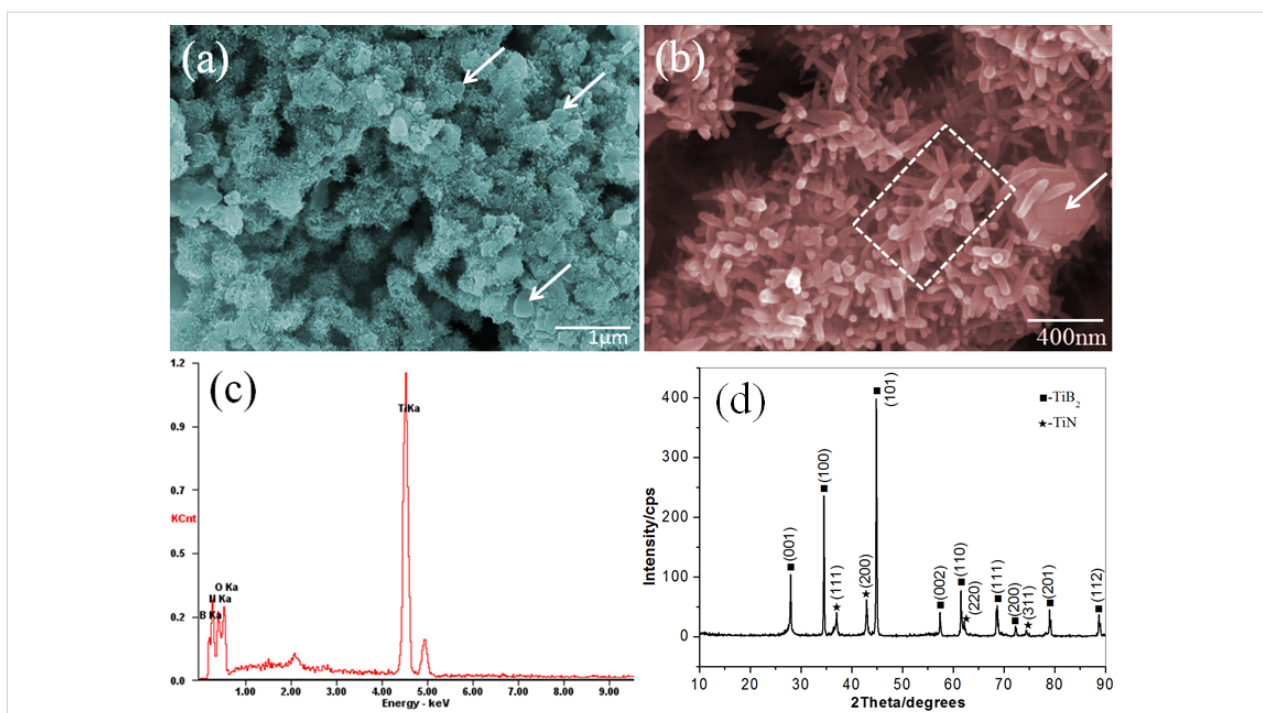


Figure 1: Typical field emission scanning electron microscope (FSEM) images (a, b), EDX spectra (c) and XRD pattern (d) of the as-synthesized $\text{TiB}_2/(\text{TiB}_2\text{-TiN})$ samples. Scale bars: (a) 1 μm and (b) 400 nm.

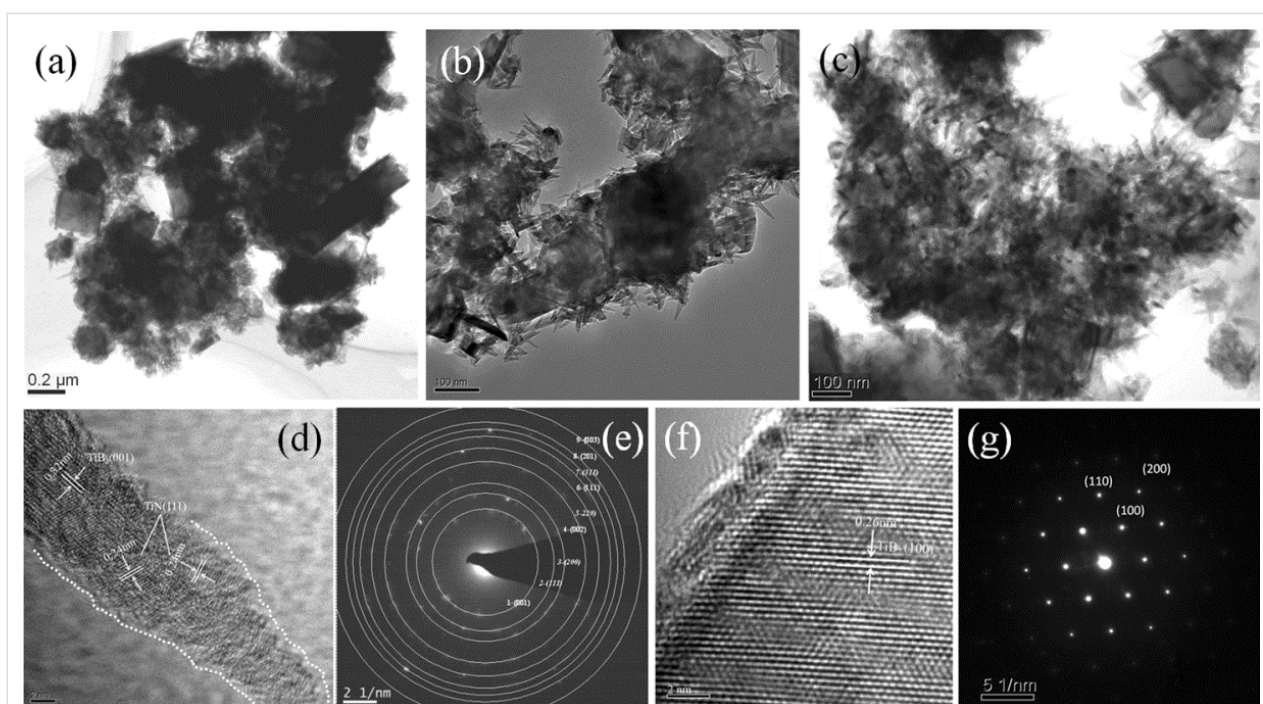


Figure 2: Typical TEM (a–c), and high-resolution TEM (d, f) images and selected-area electron diffraction (SAED) patterns (e, g) of the as-synthesized $\text{TiB}_2/(\text{TiB}_2\text{-TiN})$ samples. Scale bars: (a) 0.2 μm , (b) 100 nm, (c) 100 nm, (d) 2 nm and (f) 2 nm.

spectively. As shown in Figure 2d, the interlayer distances of the single tapered nanorod were measured as $d_1 = 0.319$ nm and $d_2 = 0.241$ nm, corresponding to the (001) plane of TiB_2 and the

(111) plane of TiN , respectively. The corresponding SAED pattern (Figure 2e) indicated that the five diffraction rings numbered 1, 4, 6, 8 and 9 were assigned to (001), (002), (111),

(201) and (003) lattice planes of TiB_2 (PDF card No.65-1073) [15]. The other four diffraction rings numbered 2, 3, 5 and 7 were attributed to (111), (200), (220) and (311) lattice planes of TiN (PDF card No.65-5774) [16].

It was worth noting that the tapered nanorods present a rough surface with abundant exposed atoms (Figure 2d), which was attributed to the different growth rates of the neighboring atom layers along the direction parallel to the crystal plane (pointed out by dash lines) [17]. It is possible that these exposed atoms could serve as high activity positions and might be used in future research in the fields of proton exchange membrane fuel cells, surface chemical modification and functionalization [18,19]. Moreover, the internal and external components were TiB_2 and TiN, respectively. The crystal planes of TiB_2 were found along the length direction of the nanorods and formed an angle with that of TiN.

As for the grains, the typical HRTEM image (Figure 2f) presented clear lattice fringes with different interplanar spacings of about 0.26 nm, which was close to that of the (100) plane of TiB_2 . The corresponding SAED pattern (Figure 2g) in-

dicated that the sample was a TiB_2 single crystal with high crystallinity. In general, the HRTEM and SAED analysis results of the hierarchical/heterostructured nanocomposites corresponded with those of the above-mentioned XRD, EDX and FSEM characterizations.

Effects of endothermic rate

Figure 3 shows typical FSEM images of the as-prepared TiB_2 -TiN samples with different endothermic rates. When the endothermic rate was 0%, the samples presented a clear typical hexagonal prism morphology of well-crystallized TiB_2 with a broad particle size of 0.02–1.5 μm (Figure 3a,b). It is worth noting that some nanoparticles (about 5 nm in diameter) existed on the surface of the hexagonal prism (pointed out by arrows in Figure 3b). When the endothermic rate reached 20%, the hexagonal prisms demonstrated slight agglomeration with the smaller particle size ranging from 200–600 nm (Figure 3c,d). Although the contour of the hexagonal prism could also be observed, the surface of the hexagonal prism became much rougher, which was attributed to the large number of nanoparticles. In addition, it was interesting that the some nanoparticles began to self-assemble into short rods (pointed out by arrows in Figure 3d).

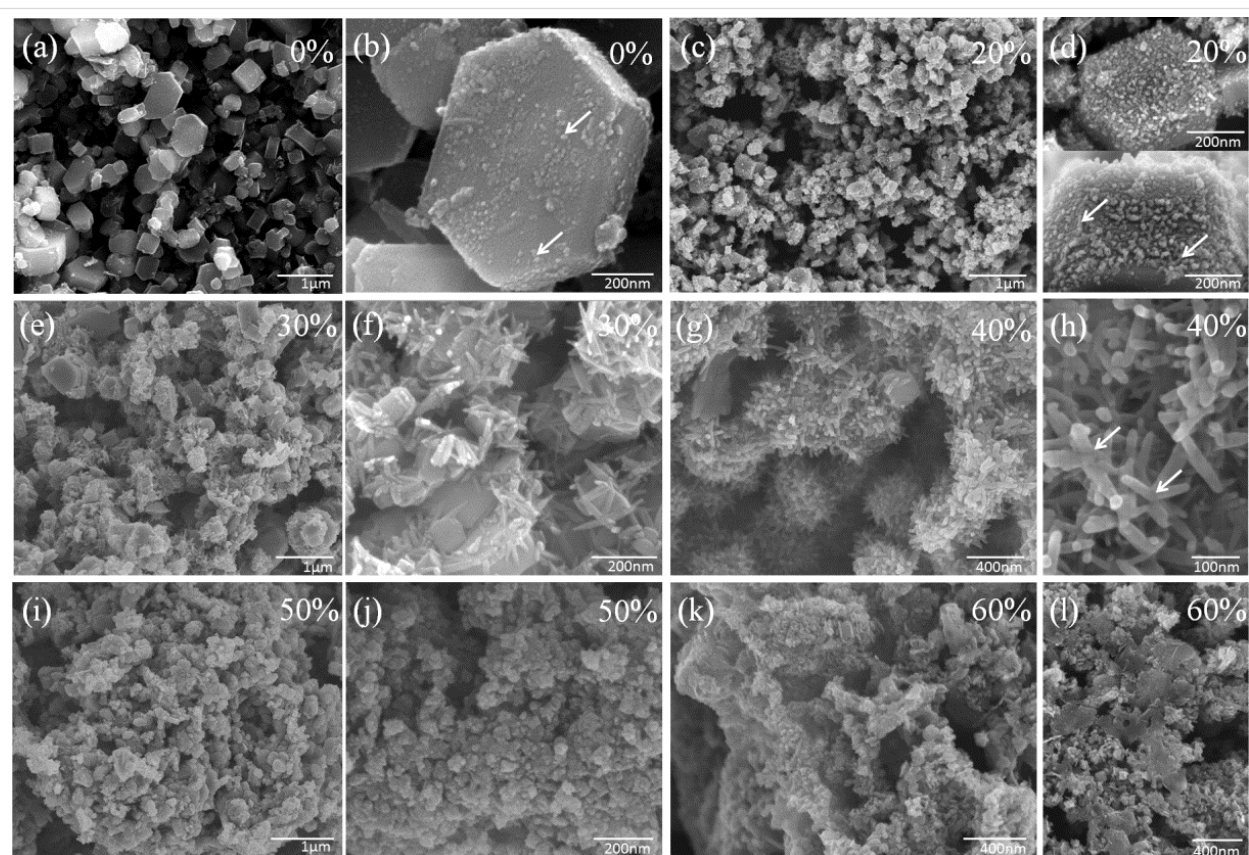


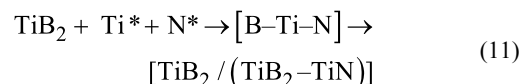
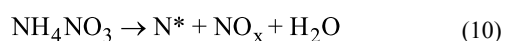
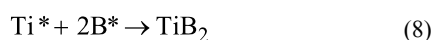
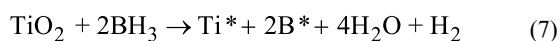
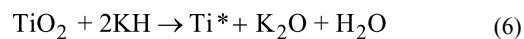
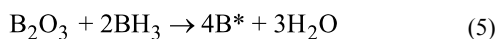
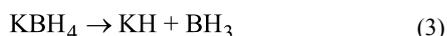
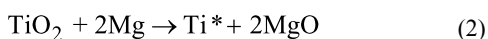
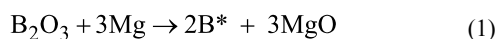
Figure 3: Typical FSEM images of the as-synthesized TiB_2 /(TiB_2 -TiN) samples with different endothermic rates (a,b) 0%; (c,d) 20%; (e,f) 30%; (g, h) 40%; (h,i) 50%; (j,k) 60%. Scale bars: (a) 1 μm , (b) 200 nm, (c) 1 μm , (d) 200 nm, (e) 1 μm , (f) 200 nm, (g) 400 nm, (h) 100 nm, (i) 1 μm , (j) 200 nm, (k) 400 nm and (l) 400 nm.

With the increase of the endothermic rate (30%), many short rods emerged on the surface of the hexagonal prisms (Figure 3e,f). With the growth of short rods, some hexagonal prisms became smaller or were completely covered with short rods. When the endothermic rate was 40%, the novel hierarchical/heterostructures emerged, which were composed of hexagonal prism grains and short rods (Figure 3g,h). Additionally, the grains that originally existed at the center of the hierarchical structures eventually disappeared completely and transformed into scattering multibranch structures (marked with arrows in Figure 3h); however, when the endothermic rate was increased to 50%, the hexagonal prisms and short rods both vanished, and only irregularly shaped particles with poor crystallinity were found (Figure 3i,j). Moreover, the higher endothermic rate (60%) led to various morphologies of samples (Figure 3k,l). It is likely that the reaction was incomplete, which then caused the generation of impurities and/or byproducts [9,10].

Given the above-mentioned comparative experimental analysis results, it could be shown that the morphology, particle size, microstructure and purity of $\text{TiB}_2/(\text{TiB}_2\text{-TiN})$ samples could be effectively controlled through the in situ reaction coupling self-propagating high-temperature synthesis (RC-SHS) method. The results were found to be in agreement with that of our previous studies [9,10,14].

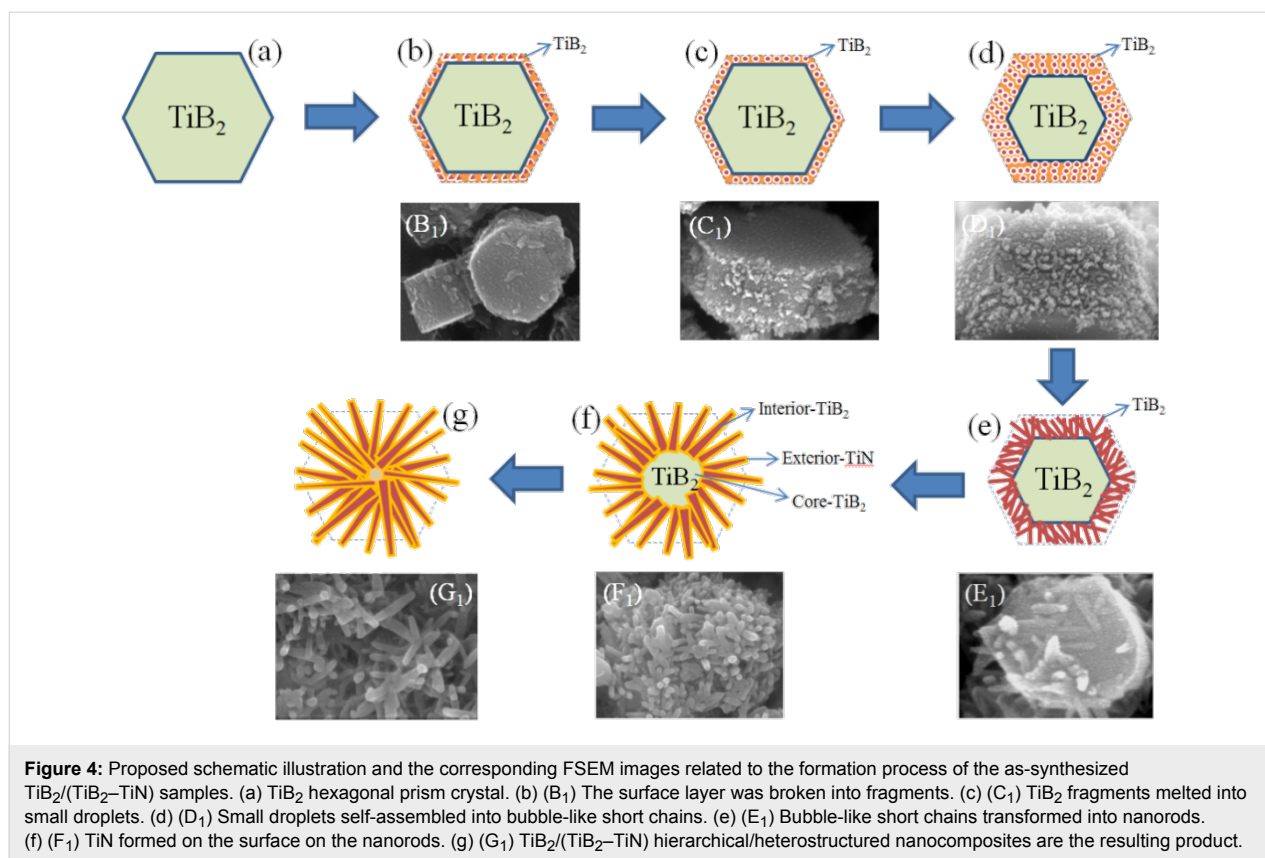
Chemical reactions and growth mechanism

During the growth process of the $\text{TiB}_2/(\text{TiB}_2\text{-TiN})$ hierarchical/heterostructured nanocomposites, the following chemical reactions are applied:



At the beginning of the RC-SHS process, the exothermic magnesium reaction occurs and produces chemically active B^* and Ti^* with a large amount of heat (Equation 1 and Equation 2) [14,20]. The heat leads to the decomposition of KBH_4 and generates KH/BH_3 with strong reduction capacity (Equation 3) [21-23]. The KH/BH_3 reacts with the residual B_2O_3 and TiO_2 , then forms B^* , Ti^* , K_2O , H_2O and H_2 (Equation 4-7). The B^* combines with Ti^* to produce TiB_2 crystals (Equation 8). KOH is also produced by the reaction between K_2O and H_2O (Equation 9) [13]. At the same time, the high temperature could promote NH_4NO_3 splitting into active N^* , NO_x and H_2O (Equation 10) [24,25]. Under the special reaction coupling self-propagating high-temperature environment, N^* and the rest of Ti^* could be deposited on the surface of the TiB_2 crystals, and finally, the novel $\text{TiB}_2/(\text{TiB}_2\text{-TiN})$ hierarchical/heterostructured nanocomposites are the product (Equation 11).

The basic principle of the self-propagating high-temperature synthesis technology has been studied for many years and has achieved some meaningful success [26,27]. However, the corresponding deeper research regarding the growth mechanism of the desired inorganic materials with hierarchical and/or heterostructures has been rarely reported. In this work, first, high quality TiB_2 hexagonal prism crystals were prepared according to the above mentioned reaction coupling self-propagating high-temperature synthesis principle (Figure 4a). The SHS reaction system creates a special environment where the surface layer of the formed TiB_2 crystals can be broken into fragments due to the infiltration and erosion of the high concentration of N^* , Ti^* and H_2 vapors (Figure 4b) [28-30]. Under high temperature, the TiB_2 fragments melted into many small droplets (Figure 4c). And the energy balance at the surface of the TiB_2 crystal depends strongly on the changes in the external environment conditions. Thus, the small droplets self-assembled into bubble-like short chains (Figure 4d) followed by rods (Figure 4e) in order to satisfy the minimized surface energy [31]. Then the N^* and the rest of the Ti^* could be co-precipitated on the surface of the TiB_2 short rods to generate the TiN outer layers (Figure 4f,g). The different atom deposition rates of the neighboring atom layers along the direction parallel to the crystal plane results in nanorods with a rough surface with abundant exposed atoms (Figure 2d) [17]. In consideration of the remarkably short time of the SHS processes, the Ti , N and B atoms would likely not have enough time to diffuse and rearrange. Consequently, the crystallinity becomes gradually worse from the outer to the inside of the TiB_2/TiN rod heterostructure (Figure 2d).



Moreover, it was obvious that the grains that were previously at the center of the as-synthesized $\text{TiB}_2/(\text{TiB}_2\text{-TiN})$ hierarchical/heterostructured nanocomposites displayed different particle sizes (Figure 5, indicated with arrows); however, the above-mentioned growth mechanism was still not be able to explain the phenomenon. In fact, the particle size of the grain depended on the size of the initially formed TiB_2 crystal. According to this peculiar small size effect [32-34], the small particle has a higher specific surface area and chemical activity than that of the large particle. Therefore, under the same conditions, the relative thickness of the infiltration and erosion layer was different between large and small particles. The smaller the TiB_2 crystals, the thicker the infiltration and erosion layers should be (Figure 5, indicated with arrows). In other words, the quantity of residual TiB_2 grain is less when the initial TiB_2 particle is small (Figure 4f). When the initially formed TiB_2 was infiltrated and eroded completely, the TiB_2 grain at the core of the hierarchical/heterostructured nanocomposites disappeared (Figure 4g), and finally, only scattering multibranch structures sharing one head were obtained (Figure 5a,e,f, marked with dashed frames).

Chemical activity

In order to study the chemical activity of the as-synthesized $\text{TiB}_2/(\text{TiB}_2\text{-TiN})$ hierarchical/heterostructured nanocomposites,

thermogravimetric and differential scanning calorimetry analyzer (TG-DSC) thermal analysis comparison experiments have been employed in flowing air. Figure 6a–c shows the TG-DSC results of three representative samples (#1 commercial high purity TiB_2 powders with an average particle size of 5 μm , #2 $\text{TiB}_2/(\text{TiB}_2\text{-TiN})$ powders of 0% endothermic rate with an average particle size of 0.9 μm , #3 $\text{TiB}_2/(\text{TiB}_2\text{-TiN})$ powders of 40% endothermic rate with an average particle size of 0.15 μm). Table 1 also summarizes the major related TG-DSC results and the average particle sizes of the samples (see Supporting Information File 1). The oxidation curves of the samples were typical of those reported in previous literature [35-38]. The oxidation process can be divided into three stages. Firstly, TiB_2 is oxidized to TiO_2 and solid B_2O_3 [36,39]. Secondly, when the temperature reaches the melting point, the B_2O_3 begins to transform into liquid [37]. The molten liquid B_2O_3 acts as a protective layer and restrains the reaction between remaining TiB_2 particle and O_2 [36,40]. Thirdly, with the increase of temperature, the evaporation of liquid B_2O_3 becomes more extensive due to its higher vapor pressure [36,37]. However, there were also some significant differences in the TG and DSC results. The oxidation of samples #1, #2 and #3 started at 463 $^\circ\text{C}$, 446 $^\circ\text{C}$ and 422 $^\circ\text{C}$ (TG plots), which correspond to the exothermic peaks of about 518 $^\circ\text{C}$ (peak #1), 490 $^\circ\text{C}$ (peak #2) and 480 $^\circ\text{C}$ (peak #3), respectively (DSC

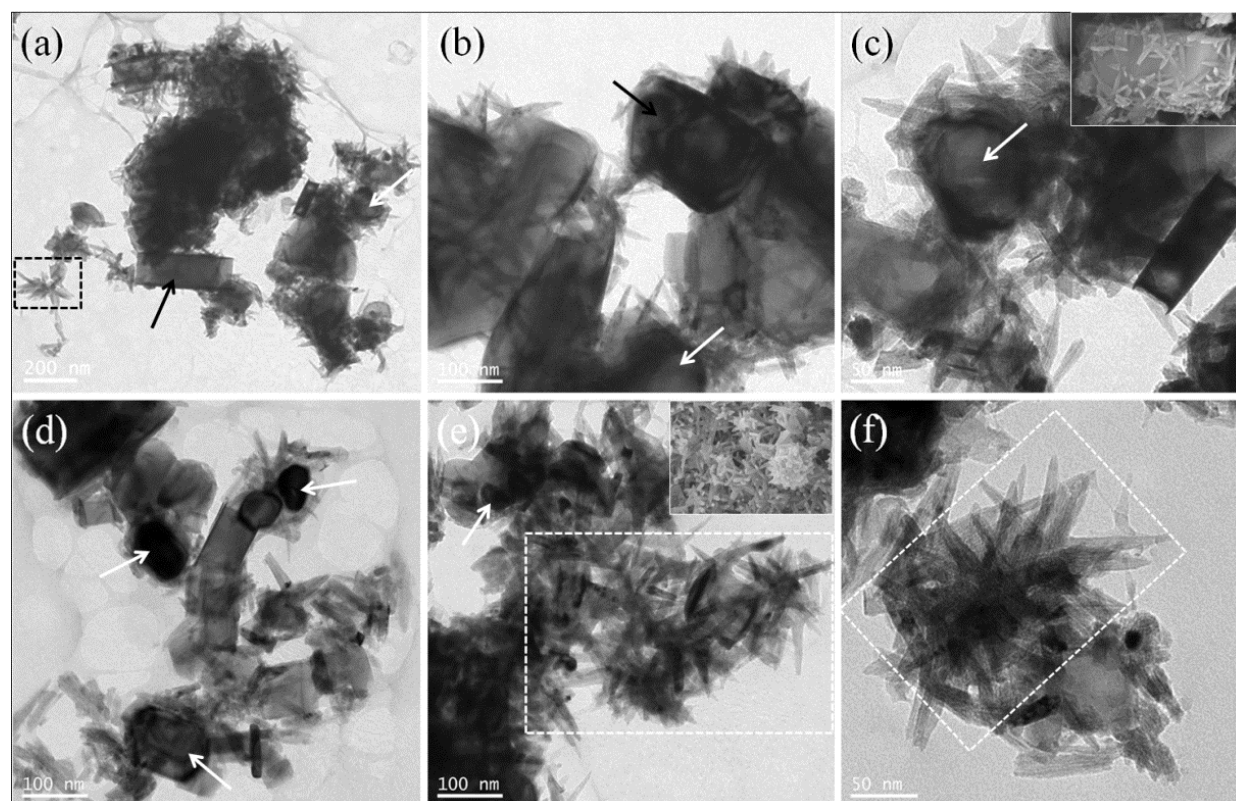


Figure 5: Typical TEM and FSEM images of the as-synthesized $\text{TiB}_2/(\text{TiB}_2\text{-TiN})$ samples with different thickness of the infiltration and erosion layers. Scale bars: (a) 200 nm, (b) 100 nm, (c) 50 nm, (d) 100 nm, (e) 100 nm and (f) 50 nm.

curves). In addition, the other weight gain temperature ranges of the three samples (#1 550–839 °C, #2 577–707 °C, #3 517–695 °C) in the TG plots were assigned as exothermic reactions at 710 °C, 644 °C and 630 °C in the DSC analysis. Besides, the proportion of the released heat for peak 1 increased in turn from sample #1, #2 to #3. The same trends were evident with the weight change from the TG analysis.

Based on the TG-DSC analysis results and the previous research, sample #3 could most easily be oxidized and revealed the highest oxidation degree, but the opposite was true for sample #1. This implies that the chemical activity sequence of the three samples was #1 < #2 < #3. In our opinion, there were three reasons that account for this phenomenon: (1) according to the peculiar small size effect, the smaller particles demonstrate higher specific surface areas than those of larger particle [32–34]; (2) the infiltration and erosion of N^* , Ti^* and H_2 vapors [28–30] in the RC-SHS process could lead to the rough metastable surface with abundant active atoms and/or defects; or (3) the novel hierarchical/heterostructured nanocomposites with a uniform particle size distribution may be favorable for improving the chemical activity of samples.

Conclusion

Novel $\text{TiB}_2/(\text{TiB}_2\text{-TiN})$ hierarchical/heterostructured nanocomposites were fabricated via a special reaction coupling self-propagating high temperature synthesis (RC-SHS) method where in situ control of the material properties was established. The as-synthesized samples consisted of TiB_2 nanograins as the core/seed and $\text{TiB}_2/(\text{TiB}_2\text{-TiN})$ composite nanorods which covered this core. The $\text{TiB}_2/(\text{TiB}_2\text{-TiN})$ composite nanorods also presented a rough surface with abundant exposed active atoms and/or defects. Additionally, based on the obtained experimental results and the previous studies, the proposed chemical reaction processes and the corresponding growth model of the hierarchical/heterostructured nanocomposites were justified. Moreover, the high chemical activity of the samples was also confirmed by TG-DSC analysis. This special highly active material could possibly be further used in the research fields of proton exchange membrane fuel cells, structural and functional performance integrated composite ceramics and/or films, surface chemical modification and functionalization.

Another point worth noting is that the detailed comparison experiments have demonstrated that the reaction coupling self-

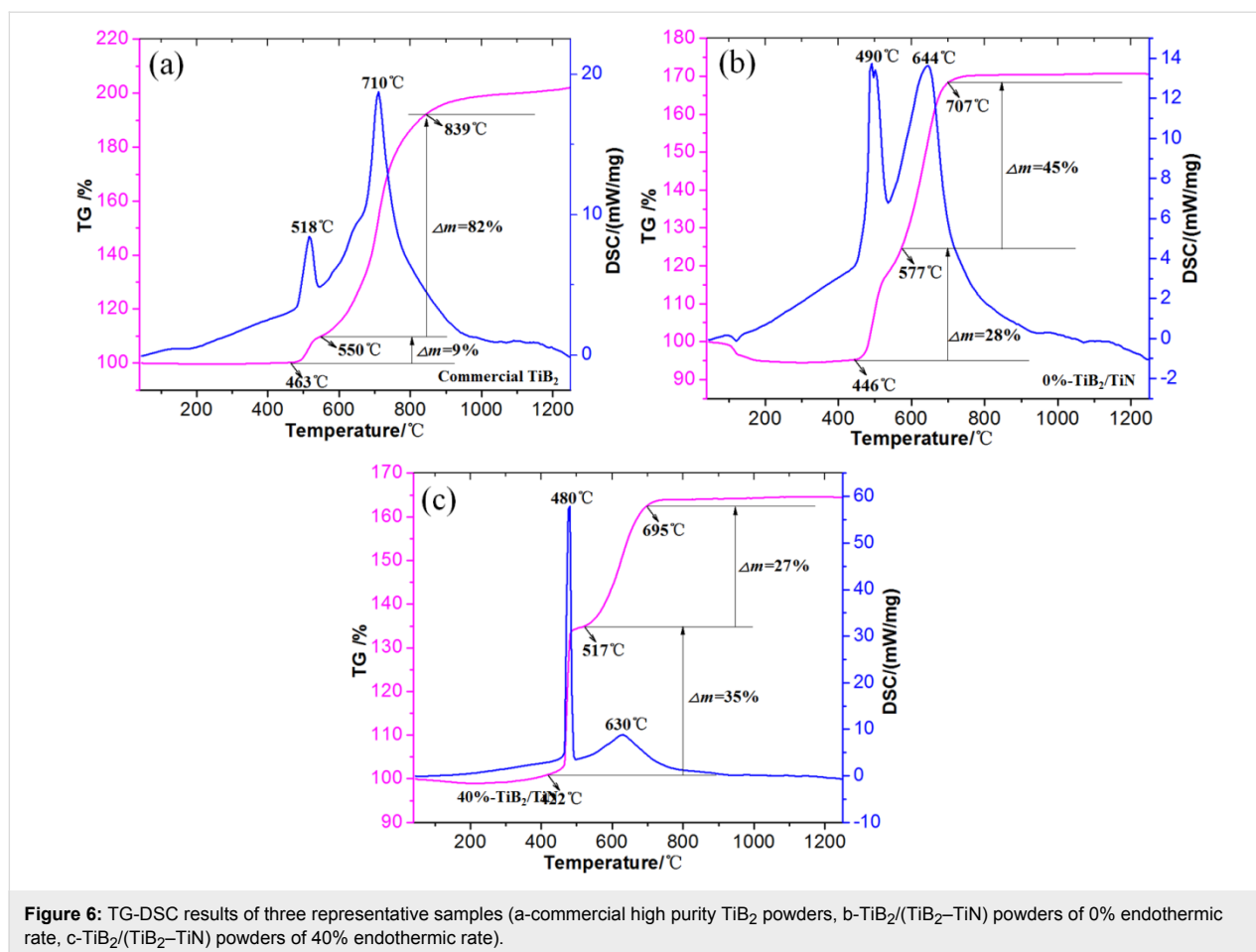


Figure 6: TG-DSC results of three representative samples (a-commercial high purity TiB_2 powders, b- $\text{TiB}_2/(\text{TiB}_2\text{-TiN})$ powders of 0% endothermic rate, c- $\text{TiB}_2/(\text{TiB}_2\text{-TiN})$ powders of 40% endothermic rate).

propagating high temperature synthesis technology could effectively be used to control the morphology, particle size, dispersibility and purity of the as-synthesized samples. Therefore, this work not only provides new experimental and theoretical evidence for the scientific rationality of this new technology, but also further expands the variety of materials available from single inorganic nanocrystals to binary hierarchical/heterostructured nanocomposites.

Experimental

Reaction coupling principles and the theoretical calculations

The reaction coupling principles have been reported in our previous work [9,10,14]. Generally, it is essential to find two kinds of reactions: one reaction is exothermic, while the other is endothermic. The heat energy of the whole RC-SHS system can be controlled by changing the endothermic reaction rate. The endothermic rate is the percentage of the resulting material (TiB_2) prepared through an endothermic reaction with respect to the total desired material (TiB_2). In this work, the two kinds of reactions could be designed as follows: Equation 12 is associated with a traditional magnesium exothermic reaction,

while Equation 13 is an endothermic reaction. The standard enthalpies of Equation 12 and Equation 13 are calculated as $-15.88 \text{ kJ}/(\text{g TiB}_2)$ and $5.89 \text{ kJ}/(\text{g TiB}_2)$, respectively. Besides, ammonium nitrate and nitrogen are applied as the nitrogen source. Finally, the whole reaction of $\text{B}_2\text{O}_3/\text{TiO}_2/\text{Mg}/\text{KBH}_4/\text{NH}_4\text{NO}_3/\text{N}_2$ can be described as follows in Equation 14.

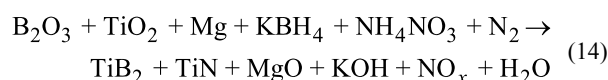
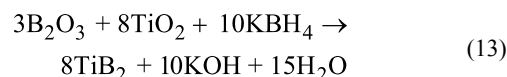
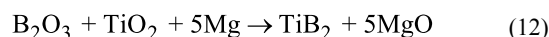
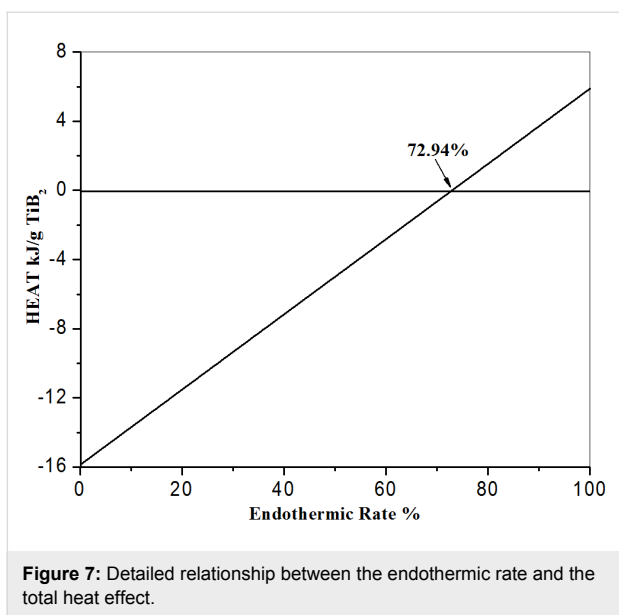


Figure 7 presents the relationship between the endothermic rate and thermal effect. When the endothermic rate reaches 72.94%, the heat effect of the whole reaction system achieves equilibrium.



Synthesis techniques

The raw materials TiO_2 , Mg, B_2O_3 , KBH_4 and NH_4NO_3 were of analytical grade and purchased from Sinopharm Chemical Reagent Co., Ltd., China without further treatment. In a typical procedure, TiO_2 , Mg and B_2O_3 were milled for 2 h by a planet-type ball mill (the weight rate between stainless steel ball and mixture powders was 30:1, rotating rate was 250 rpm). The obtained milled products were mixed with KBH_4 and NH_4NO_3 . Then the mixture (mole ratio B/Ti/N was 2.65:1.34:0.7) was pressed into a cylinder with a diameter of 30 mm. The cylinder was heated in a nitrogen atmosphere at 700–850 °C for 8–15 min in a self-designed SHS furnace. After cooling to room temperature naturally, the crude product was collected and washed with hydrochloric acid, ethanol and distilled water. Finally, $\text{TiB}_2/(\text{TiB}_2\text{--TiN})$ nanocomposite powders were collected by drying in vacuum at 80 °C for 24 h.

Characterization

The phase structure of the samples was characterized using powder X-ray diffraction (XRD) with Cu $K\alpha$ radiation. The morphology and microstructure of the samples were investigated using a Hitachi S4800 field emission scanning electron microscope (FSEM), a Philips CM12 transmission electron microscope (TEM), a JEOL JEM-2100F high-resolution transmission electron microscope (HRTEM) and the selected-area electron diffraction (SAED) instrument attached on the Philips CM12 TEM. The elemental composition and content of the samples was analyzed using an X-ray energy dispersive spectroscopy (EDX) attached to the S4800 FSEM. The chemical activity of the samples was measured with the help of the Netzsch STA 449F3 thermogravimetric and differential scanning calorimetry analyzer (TG-DSC) at a heating rate of 10 °C/min.

Supporting Information

Supporting Information File 1

Additional TG-DSC results.

[<http://www.beilstein-journals.org/bjnano/content/supplementary/2190-4286-8-211-S1.pdf>]

Acknowledgments

The authors acknowledge the financial support from the Program for Guangxi Natural Science Foundation (No. 2014GXNSFFA118004 and No. 2016GXNSFBA380155), Improving the Basic Ability of Young and Middle-aged University Teachers in Guangxi (No. KY2016YB187) and Opening Fund of the Guangxi Key Laboratory of Building New Energy and Energy Saving (No. 16-J-21-10).

References

- Yeh, C. L.; Teng, G. S. *J. Alloys Compd.* **2006**, *417*, 109–115. doi:10.1016/j.jallcom.2005.09.040
- Yang, Z.-L.; Ouyang, J.-H.; Liu, Z.-G.; Liang, X.-S. *Ceram. Int.* **2010**, *36*, 2129–2135. doi:10.1016/j.ceramint.2010.05.019
- Li, J. L.; Hu, K.; Zhou, Y. *Mater. Sci. Eng., A* **2002**, *326*, 270–275. doi:10.1016/S0921-5093(01)01499-X
- Karthiselva, N. S.; Bakshi, S. R. *Mater. Sci. Eng., A* **2016**, *663*, 38–48. doi:10.1016/j.msea.2016.03.098
- Karimi, Y.; Mehdipoor, A.; Alizadeh, A. *Ceram. Int.* **2016**, *42*, 11543–11547. doi:10.1016/j.ceramint.2016.03.232
- Turan, A.; Bugdayci, M.; Yucel, O. *High Temp. Mater. Processes (Berlin, Ger.)* **2015**, *34*, 185–193. doi:10.1515/htmp-2014-0021
- Khobta, I.; Petukhov, O.; Vasyilkiv, O.; Sakka, Y.; Ragulya, A. *J. Alloys Compd.* **2011**, *509*, 1601–1606. doi:10.1016/j.jallcom.2010.10.198
- Shim, J.-H.; Byun, J.-S.; Cho, Y. W. *Scr. Mater.* **2002**, *47*, 493–497. doi:10.1016/S1359-6462(02)00188-4
- Wang, J.; Long, F.; Wang, W.; Mo, S.; Zou, Z.; Fu, Z. *Ceram. Int.* **2016**, *42*, 6969–6977. doi:10.1016/j.ceramint.2016.01.083
- Da, A.; Long, F.; Wang, J.; Xing, W.; Wang, Y.; Zhang, F.; Wang, W.; Fu, Z. *J. Wuhan Univ. Technol., Mater. Sci. Ed.* **2015**, *30*, 729–734. doi:10.1007/s11595-015-1220-8
- Gutmanas, E. Y.; Gotman, I. *J. Eur. Ceram. Soc.* **1999**, *19*, 2381–2393. doi:10.1016/S0955-2219(99)00104-1
- Shibuya, M.; Ohyanagi, M.; Munir, Z. A. *J. Am. Ceram. Soc.* **2002**, *85*, 2965–2970. doi:10.1111/j.1151-2916.2002.tb00564.x
- Yeh, C. L.; Teng, G. S. *J. Alloys Compd.* **2006**, *424*, 152–158. doi:10.1016/j.jallcom.2005.12.086
- Wang, J.; Gu, Y.; Li, Z.; Wang, W.; Fu, Z. *Mater. Res. Bull.* **2013**, *48*, 2018–2022. doi:10.1016/j.materresbull.2013.01.053
- Otani, S.; Ishizawa, Y. *J. Cryst. Growth* **1994**, *140*, 451–453. doi:10.1016/0022-0248(94)90327-1
- Kieffer, R.; Nowotny, H.; Etmayer, P.; Dufek, G. *Metall* **1972**, *26*, 701–708.
- Wang, J.; Zhang, L.; Long, F.; Wang, W.; Gu, Y.; Mo, S.; Zou, Z.; Fu, Z. *RSC Adv.* **2016**, *6*, 23272–23278. doi:10.1039/C6RA02475K

18. Yin, S.; Mu, S.; Lv, H.; Cheng, N.; Pan, M.; Fu, Z. *Appl. Catal., B* **2010**, *93*, 233–240. doi:10.1016/j.apcatb.2009.09.034
19. Yin, S.; Mu, S.; Pan, M.; Fu, Z. *J. Power Sources* **2011**, *196*, 7931–7936. doi:10.1016/j.jpowsour.2011.05.033
20. Zarrinpour, H.; Firoozi, S.; Milani, V. *Ceram. Int.* **2016**, *42*, 11217–11223. doi:10.1016/j.ceramint.2016.04.032
21. Hu, J.-Q.; Lu, Q.-Y.; Tang, K.-B.; Yu, S.-H.; Qian, Y.-T.; Zhou, G.-E.; Liu, X.-M.; Wu, J.-X. *J. Solid State Chem.* **1999**, *148*, 325–328. doi:10.1006/jssc.1999.8454
22. Sun, G.; Gao, F.; Hou, L. *Can. J. Chem.* **2010**, *88*, 1256–1261. doi:10.1139/V10-146
23. Wu, Y.; Ni, Y. *Chem. Eng. J.* **2012**, *187*, 328–333. doi:10.1016/j.cej.2012.01.075
24. Cagnina, S.; Rotureau, P.; Singh, S.; Turcotte, R.; Fayet, G.; Adamo, C. *Ind. Eng. Chem. Res.* **2016**, *55*, 12183–12190. doi:10.1021/acs.iecr.6b02834
25. Mihai, O.; Tamm, S.; Stenfeldt, M.; Olsson, L. *Philos. Trans. R. Soc., A* **2016**, *374*, 20150086. doi:10.1098/rsta.2015.0086
26. Huczko, A.; Kurcz, M.; Dabrowska, A.; Baranowski, P.; Bhattarai, A.; Gierlotka, S. *J. Cryst. Growth* **2014**, *401*, 469–473. doi:10.1016/j.jcrysgro.2014.02.049
27. Levashov, E. A.; Mukasyan, A. S.; Rogachev, A. S.; Shtansky, D. V. *Int. Mater. Rev.* **2017**, *62*, 203–239. doi:10.1080/09506608.2016.1243291
28. Zhong, B.; Huang, X. X.; Wen, G. W.; Qin, C. L.; Zhang, X. D.; Bai, H. W. *Mater. Res. Bull.* **2011**, *46*, 970–974. doi:10.1016/j.materresbull.2011.02.020
29. Wang, J.; Li, Z.; Gu, Y.; Du, X.; Zhang, Z.; Wang, W.; Fu, Z. *Ceram. Int.* **2015**, *41*, 1891–1896. doi:10.1016/j.ceramint.2014.09.032
30. Wang, J.; Peng, D.; Long, F.; Wang, W.; Gu, Y.; Mo, S.; Zou, Z.; Fu, Z. *Solid State Sci.* **2017**, *64*, 23–28. doi:10.1016/j.solidstatesciences.2016.12.001
31. Huang, F.; Fu, Z.; Yan, A.; Wang, W.; Wang, H.; Wang, Y.; Zhang, J.; Cheng, Y.; Zhang, Q. *Cryst. Growth Des.* **2009**, *9*, 4017–4022. doi:10.1021/cg900161w
32. Goldstein, A. N.; Echer, C. M.; Alivisatos, A. P. *Science* **1992**, *256*, 1425–1427. doi:10.1126/science.256.5062.1425
33. Chopra, N. G.; Luyken, R. J.; Cherrey, K.; Crespi, V. H.; Cohen, M. L.; Louie, S. G.; Zettl, A. *Science* **1995**, *269*, 966–967. doi:10.1126/science.269.5226.966
34. Huo, K. F.; Hu, Z.; Fu, J. J.; Xu, H.; Wang, X. Z.; Chen, Y.; Lü, Y. N. *J. Phys. Chem. B* **2003**, *107*, 11316–11320. doi:10.1021/jp035375w
35. Voitovich, V. B.; Lavrenko, V. A.; Golovko, E. I.; Adejev, V. M. *Oxid. Met.* **1994**, *42*, 249–263. doi:10.1007/BF01052026
36. Chen, L.; Gu, Y.; Qian, Y.; Shi, L.; Yang, Z.; Ma, J. *Mater. Res. Bull.* **2004**, *39*, 609–613. doi:10.1016/j.materresbull.2003.12.005
37. Shahbahrani, B.; Bastami, H.; Shahbahrani, N. *Mater. Res. Innovations* **2010**, *14*, 107–109. doi:10.1179/143307510X12599329343204
38. Blokhina, I. A.; Ivanov, V. V. *J. Therm. Anal. Calorim.* **2015**, *119*, 123–130. doi:10.1007/s10973-014-4196-2
39. Koh, Y.-H.; Lee, S.-Y.; Kim, H.-E. *J. Am. Ceram. Soc.* **2001**, *84*, 239–241. doi:10.1111/j.1151-2916.2001.tb00641.x
40. Senda, T. *J. Ceram. Soc. Jpn.* **1996**, *104*, 785–787. doi:10.2109/jcersj.104.785

License and Terms

This is an Open Access article under the terms of the Creative Commons Attribution License (<http://creativecommons.org/licenses/by/4.0>), which permits unrestricted use, distribution, and reproduction in any medium, provided the original work is properly cited.

The license is subject to the *Beilstein Journal of Nanotechnology* terms and conditions: (<http://www.beilstein-journals.org/bjnano>)

The definitive version of this article is the electronic one which can be found at:
doi:10.3762/bjnano.8.211